CFD Simulations and Particle Image Velocimetry Measurements in an Industrial Scale Rotating Disc Contactor

Christian Drumm, Mark W. Hlawitschka, and Hans-Jörg Bart
Lehrstuhl für Thermische Verfahrenstechnik, TU Kaiserslautern, Center of Mathematical and Computational Modeling, TU Kaiserslautern, Kaiserslautern 67653, Germany

DOI 10.1002/aic.12249
Published online April 20, 2010 in Wiley Online Library (wileyonlinelibrary.com).

Fluid dynamics of the single-phase and two-phase flow in a segment of a rotating disc contactor (RDC) liquid–liquid extraction column with 450 mm inner diameter were studied by performing computational fluid dynamics (CFD) simulations and particle image velocimetry (PIV) measurements. The fluid dynamics were investigated to test the predictivity of CFD at industrial scale. Different turbulence models in conjunction with the Eulerian approach were applied in the single-phase and two-phase simulations. The turbulent flow characteristics were analyzed by PIV measurements to validate the CFD simulations. An iso-optical system composed of $CaCl_2$/water–butylacetate allows for the two-phase PIV measurements. Local turbulent energy dissipation was derived from velocity gradients in PIV data. In this connection, the influence of the PIV spatial resolution on the measured energy dissipation was also analyzed, and different fit functions were tested to scale the measured energy dissipation. Simulated velocity fields as well as the energy dissipation were compared with the experimental PIV data. The results from the simulations and experiments are in good agreement. The work shows that CFD can predict hydrodynamic characteristics even at bigger scales but is still subject to some minor restrictions. © 2010 American Institute of Chemical Engineers *AIChE J,* 57: 10–26, 2011

Keywords: particle image velocimetry, liquid–liquid extraction, CFD, energy dissipation, rotating disc contactor

Introduction

Liquid–liquid extraction is a separation process, which is based on the different distribution of the separable components between two liquid phases. The process is used primarily when distillation is impractical or too costly to use.[1,2] This unit operation is widely applicable in chemical, biochemical industries, pharmacy, and hydrometallurgy. In most modern extraction processes, mechanically agitated columns as pulsed or stirred columns are applied. Stirred extraction columns can range from simple rotating disc contactor (RDC) to complicated stirrer geometry as in Kühni columns.

The use of computational fluid dynamics (CFD) software in many materials processing industries has grown tremendously in recent years. CFD has been widely used for conducting virtual experiments, prototype testing, and parametric studies. Analysis using CFD complements and reduces physical testing, and it can result in a significant time and cost saving.[3]

In the field of liquid–liquid extraction, CFD can predict fluid dynamics and turbulence and gives a fully resolved local resolution of the two-phase flow in an apparatus. It can be used as an aid to scale-up processes from laboratory or pilot scale to full production. In practice, the layout of

Correspondence concerning this article should be addressed to H.-J. Bart at bart@mv.uni-kl.de.

extractors is mainly based on the experience and empirical or semi-empirical models.

In literature, some good progress has been made in determining stirred column design parameters using CFD simulations both in single-phase[4–8] and two-phase mode.[9–13] Recent work has also dealt with liquid–liquid problems in pulsed extraction columns.[14,15] Main focus in these references is on the investigation of single-phase and two-phase velocity fields and flow patterns and residence time distribution studies for the evaluation of the axial dispersion. Comparisons to experimental particle image velocimetry (PIV),[12] laser Doppler velocimetry (LDV),[4] and laser Doppler anenometry (LDA)[5,10] data could show that CFD is a suitable design tool for the prediction of the hydrodynamic phenomena such as flow patterns, velocities, and backmixing. Only PIV allows the comparison of the whole velocity field, whereas only discrete points can be compared with LDA and LDV measurements.

Over the last years, the Euler–Euler approach emerged as the standard approach to model multiphase problems at higher hold-up and was successfully applied to model stirred RDC extractors of various geometries.[5,10–12] The Euler–Lagrange approach, also known as the discrete phase model, is best used for flow regimes where the difference between the volume fractions of the two phases is large. Therefore, the Euler–Lagrange approach was mainly applied to determine dispersion coefficients from a small amount of droplets but fails to predict column behavior at higher hold-up (above 10%).[5,7] Nevertheless, the model was applied by other authors to simulate stirred extraction columns at this lower hold-up.[16,17]

Generally, it is sufficient to apply a two-fluid model in CFD for the description of the dispersed liquid–liquid problem.[12,18] Drop size distributions in liquid–liquid extractors are usually monomodal and narrow and drop sizes range from around 1 to 5 mm. In this connection, the Sauter mean diameter represents the different sizes of the particles in the dispersed phase, whereas the influence of the size-specific terminal velocity resulting from the drop size distribution could be neglected. Multifluid models are highly CPU time consuming and are only necessary for wide or multimodal distributions. The coupling of CFD and population balance modeling (PBM) is another promising alternative for an advanced modeling of dispersed multiphase systems.[19] CFD can predict the hydrodynamics and turbulence and give a fully developed local resolution of the two-phase flow in all three external coordinates, whereas the PBM can account for the droplet coalescence and breakup and analyze the size distribution of the dispersed phase. Nevertheless, these coupled solvers stand and fall with the correct prediction of the fluid dynamics.

In the previous work, the single-phase and two-phase flow field of a RDC pilot plant column (150 mm inner diameter) was simulated by means of CFD.[12,19,20] The single-phase and two-phase simulations were validated by PIV measurements. These were the first works that could validate the whole flow field in single-phase and two-phase operational mode instead of comparing only discrete points as with LDA measurements. In all given citations, CFD was applied for the simulation of pilot scale or lab-scale columns. On the other hand, industrial scale CFD simulations are hardly found because of the high computational load.

Table 1. Dimensions of the RDC Geometry

		RDC DN150	RDC DN450
Column diameter (mm)	D_K	150	450
Diameter shaft (mm)	D_{shaft}	54	54
Compartment height (mm)	H_C	30	90
Height stirrer/stator (mm)	H_R	1	3
Diameter stirrer (mm)	D_R	90	270
Stator inner diameter (mm)	D_s	105	315

Therefore, in the present work, the applicability of CFD is tested for an industrial scale RDC extraction column. An industrial scale (450 mm inner diameter) test rig with three extraction compartments is investigated. The predictivity of CFD simulations for the bigger scale can be estimated. PIV measurements are conducted in single-phase and two-phase mode for validation and are compared with the CFD simulations. The aim of this study is to predict the velocity fields in the aqueous phase for the different scales in single-phase and two-phase (countercurrent) flow and to investigate the distribution of energy dissipation in the extraction compartment, which is one of the most important parameters in liquid–liquid extraction modeling. Stagnant or dead zones of the flow field are also observed in CFD and PIV and are compared with each other. Main focus is on the correct prediction of the fluid dynamics and turbulence also to guarantee a successful future coupling with PBM. In PBM, the breakage and coalescence kernels are usually strong functions of the energy dissipation. Especially, breakage is mainly occurring in the stirrer outflow. That is why, for the local energy dissipation, the main focus is on this region. In future, with increasing computational power, full-scale CFD simulations could be possible without scale-up steps.

The article is structured as follows: first, the experimental setup and the computational model are described briefly. The results of the CFD simulations and the comparison to the experimental data are presented in the main part of the article. Single-phase flow results and the analysis of the energy dissipation are followed by the two-phase results. At the end of the article, summary and conclusions are given.

Experimental Setup

Rotating disc contactor

The RDC is the most commonly used extractor for aromatics extraction in the petrochemical industry. The previously investigated pilot plant column with an inner diameter of 150 mm is often applied for scale-up purposes.[12] The layout rule by Kosters[21] was applied for the scale-up of the RDC geometry of a DN450 column. Diameter of the shaft was held constant to avoid a 160-mm shaft. The resulting measurement area in the 450 mm test rig is around 10 times larger as in the 150 mm column. The dimensions are compared in Table 1. A sketch of the RDC geometry is given in Figure 1. Three RDC compartments were installed in the test rig with an overall height of around 1 m. The column can be operated at one-phase and two-phase conditions, the aqueous phase entering at the top and leaving at the bottom. A perforated pipe at the bottom of the column served as the dispersed phase distributor, which generates droplets in the mm

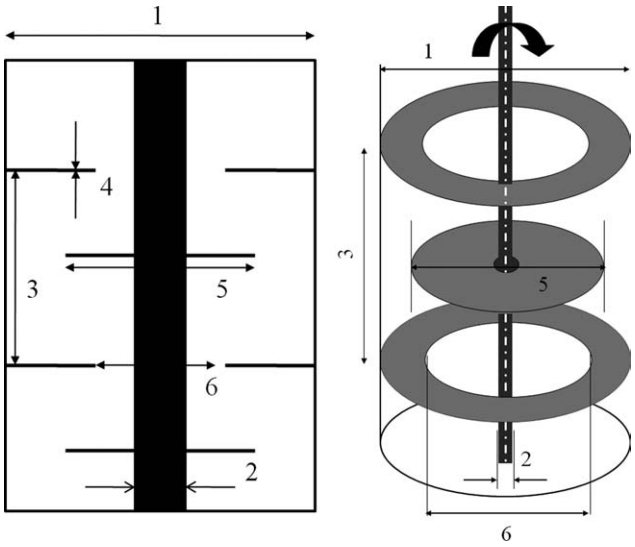

Figure 1. RDC geometry.

range. Variable rotation of the disc stirrers is warranted by an agitator. Different rotational speeds (50, 100, 150, 200, and 300 rpm) were investigated in the test rig. The volume flow of the phases was 1000 L/h in single-phase operating mode and 500 L/h per phase in two-phase mode. The drop sizes in the column were determined from digital photos. The drop size was determined as the Sauter mean diameter ($d_{32} = \sum n_i d_i^3 / \sum n_i d_i^2$) where n_i is the number of identified droplets. The d_{32} was estimated around 2 mm (300 rpm) and 3 mm (100 rpm).

PIV technique

Velocity measurements and the estimation of the turbulent energy dissipation are needed for a comparison with the CFD simulations. PIV measurements are conducted for the validation of the simulations. The PIV technique allows the recording of a complete flow velocity field in a plane of the flow within a few microseconds.[22] Some key data of the PIV setup are given in this chapter. A detailed description of the PIV setup was also given in previous work.[12,20]

An intelligent laser applications (ILA GmbH) 2D PIV system was used. It includes a pair of Nd:YAG lasers, the CCD camera (PCO SensiCam, 1280 × 1024 px^2) and the ILA synchronizer. The flow is seeded with small tracer particles that follow the flow. A cross section of the flow is illuminated with the use of a laser light sheet. The CCD camera is used to record images of the particles in the illuminated plane. Two subsequent images of the flow separated by a short time delay, Δt, are divided into small interrogation areas. In the time interval between light pulses, the particles move a short distance. Their displacements are then calculated and can be converted into a velocity vector field by cross correlation when knowing the pulse separation and the image scale. ILA's VidPIV software version 4.6XP was applied for the data analysis. A linear mapping was used to assign the pixels of a picture to physical units. The pulse distance was varied between 250 and 1500 μs. The interrogation areas for the cross correlation were 64 × 64 pixel with a 50% overlapping, followed by an 32 × 32 pixel adaptive cross correlation. The erroneous vectors were removed and replaced by a global velocity filter and local 3 × 3 median filters. The outliers were finally interpolated to fill the holes in the vector field. Images were captured at a rate of 4 Hz for 50 s. Two hundred pairs of pictures were taken for the determination of ensemble-averaged velocity fields.

For the single-phase water experiments, polyamide tracer particles with a diameter of 50 μm and a density of 1060 kg/m^3 were applied. The density difference between the particles and the water phase and the resulting errors can be neglected. In a two-phase liquid–liquid flow, the presence of the dispersed phase introduces problems to the PIV method, which are not present in single-phase flows. The dispersed phase masks the measurement plane and a clear view on the illuminated plane is not possible. For the two-phase PIV, a refractive index matching technique is the method of choice.[12] The measurement of the aqueous phase velocities is possible by the use of an iso-optical system, where the refractive index of both liquid phases is identical. In this work, a system with matching refractive indices was applied that allows the discrimination of the phases and makes an estimation of the phase fractions possible. The system is composed of butylacetate as the dispersed phase and a calcium chloride/water mixture (30/70 wt %) as the continuous aqueous phase. The density of the continuous and the dispersed phases were 1300 and 880 kg/m^3, respectively. The viscosity of both phases is 0.02 and 0.00074 kg/ms. The fluorescent dye Rhodamine 6G only soluble in the aqueous phase allows the discrimination of the phases. Hollow glass spheres with a diameter of 10 μm and a density of 1100 kg/m^3 only soluble in the aqueous phase seeded the two-phase flow.

The RDC compartment was divided into different zones to increase the resolution of the PIV measurements. The measurement areas are shown in Figure 2. Zone 1 ranges from the stirrer to the wall and a second zone around the stirrer was chosen for the estimation of the turbulent energy dissipation. The dimensions of Zone 1 are obvious from Table 1 and Figure 1. The dimensions of Zone 2 are given in mm in Figure 2. It was also attempted to measure the area between the shaft and the stirrer tip (left side of the compartment in

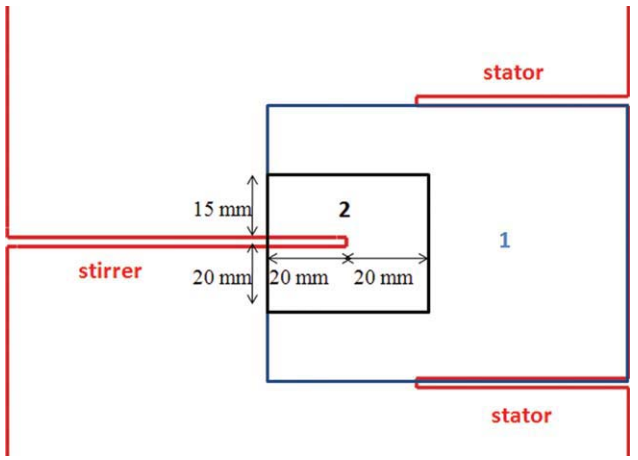

Figure 2. PIV measurement areas.

[Color figure can be viewed in the online issue, which is available at wileyonlinelibrary.com.]

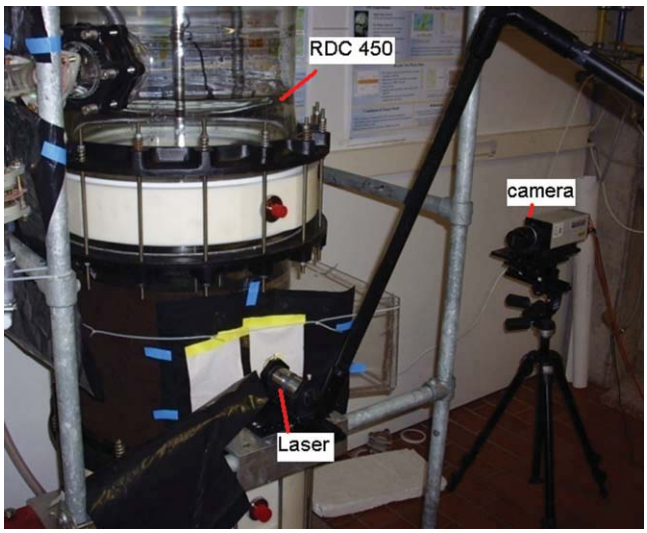

Figure 3. PIV setup.

[Color figure can be viewed in the online issue, which is available at wileyonlinelibrary.com.]

Figure 2). Unfortunately, the illumination of the tracer particles and the overall picture quality in the dense system were not good enough to guarantee reliable measurements. A photograph of the PIV setup is shown in Figure 3.

Turbulent energy dissipation

PIV offers the possibility to estimate turbulent kinetic energy k and its dissipation rate ε. The approach is shortly described here. The determination of dissipation rate through direct PIV measurement of fluctuating velocity gradients is widely investigated and further information could be found in relevant literature.[23–27]

The turbulent kinetic energy and its dissipation rate are derived from the fluctuating velocities and their spatial derivatives. First, the ensemble-averaged velocity field $\overline{u}$ is subtracted from the instantaneous velocity fields u to obtain the local fluctuating velocity fields u' in VidPIV.

$$u' = u - \bar{u} \tag{1}$$

The local energy dissipation ε can be written as follows:

$$\varepsilon = \upsilon \left[\begin{array}{l} 2\left(\overline{\left(\frac{\partial u_i'}{\partial x_i}\right)^2} + \overline{\left(\frac{\partial u_j'}{\partial x_j}\right)^2} + \overline{\left(\frac{\partial u_k'}{\partial x_k}\right)^2}\right) + \overline{\left(\frac{\partial u_i'}{\partial x_j}\right)^2} + \overline{\left(\frac{\partial u_j'}{\partial x_i}\right)^2} + \overline{\left(\frac{\partial u_i'}{\partial x_k}\right)^2} + \\ \overline{\left(\frac{\partial u_k'}{\partial x_i}\right)^2} + \overline{\left(\frac{\partial u_j'}{\partial x_k}\right)^2} + \overline{\left(\frac{\partial u_k'}{\partial x_j}\right)^2} + 2\left(\overline{\left(\frac{\partial u_i'}{\partial x_j}\frac{\partial u_j'}{\partial x_i}\right)} + \overline{\left(\frac{\partial u_i'}{\partial x_k}\frac{\partial u_k'}{\partial x_i}\right)} + \overline{\left(\frac{\partial u_j'}{\partial x_k}\frac{\partial u_k'}{\partial x_j}\right)}\right) \end{array} \right] \tag{2}$$

where υ is the kinematic viscosity.

Only five of the 12 terms can be determined from 2D PIV measurements. The remaining seven terms can be obtained by using the local isotropy hypothesis.[25] Therefore, the equation for ε, in cylindrical coordinates, becomes:

$$\varepsilon = \upsilon \left[2\overline{\left(\frac{\partial u_r'}{\partial r}\right)^2} + 2\overline{\left(\frac{\partial u_z'}{\partial z}\right)^2} + 3\overline{\left(\frac{\partial u_r'}{\partial z}\right)^2} + 3\overline{\left(\frac{\partial u_z'}{\partial r}\right)^2} + 2\overline{\frac{\partial u_r'}{\partial z}\frac{\partial u_z'}{\partial r}} \right] \tag{3}$$

The fluctuating velocity fields were exported to Tecplot. Tecplot is a visualization tool, which can analyze complex data. It also serves as a CFD postprocessing software.

In Tecplot, the velocity gradients were derived and the energy dissipation was determined.

The turbulent kinetic energy k can also be estimated by a 2D approximation under isotropic flow conditions:

$$k = \frac{1}{2}\left(\tilde{u}_i^2 + \tilde{u}_j^2 + \tilde{u}_z^2\right) = \frac{3}{4}\left(\tilde{u}_i^2 + \tilde{u}_j^2\right), \tag{4}$$

where $\tilde{u}_i$ are the root-mean-square values of the instantaneous fluctuating velocity components u_i'.

To fully resolve the spatial behavior of the turbulence quantities of a turbulent three-dimensional flow field, it is necessary to measure down to the Kolmogorov length scale[26]:

$$\eta = \left(\frac{\nu^3}{\varepsilon}\right)^{1/4}. \tag{5}$$

Therefore, for the determination of the turbulent energy dissipation, an additional adaptive cross correlation with a 16 × 16 pixels interrogation area was carried out in VidPIV to improve the spatial resolution. The resulting vector field has a resolution of 8 × 8 pixels because of the 50% overlap.

Computational Model

The simulations were carried out in the CFD code Fluent 6.3. The fluid dynamics of the single-phase water phase was computed by solving the Reynolds-averaged Navier–Stokes equations. For modeling the two-phase system, an Eulerian–Eulerian two-fluid approach is used. The conservation equations of continuity and momentum are solved for each phase. The continuity equation for the liquid phase l is:

$$\frac{\partial(\alpha_l \rho_l)}{\partial t} + \nabla \times (\alpha_l \rho_l u_l) = 0, \tag{6}$$

where α is the volume fraction, which represents the space occupied by each phase, ρ is the phase density, and u is the phase velocity. The conservation of momentum for phase l is:

$$\frac{\partial(\alpha_l \rho_l u_l)}{\partial t} + \nabla \times (\alpha_l \rho_l u_l u_l) - \nabla \times \tau_l = -\alpha_l \nabla p + \alpha_l \rho_l g + F_{\mathrm{k}}, \tag{7}$$

where τ is the stress–strain tensor, p is the pressure shared by all phases, g is the gravitational acceleration, and F represents the interfacial forces.

In addition, the constraint for the volume fractions must also be satisfied in the two-phase simulations:

$$\alpha_1 + \alpha_2 = 1. \tag{8}$$

For the two-phase flow, the interphase interaction term F_{k} consists of different momentum exchange mechanisms. Only the drag force was taken into account, whereas the virtual

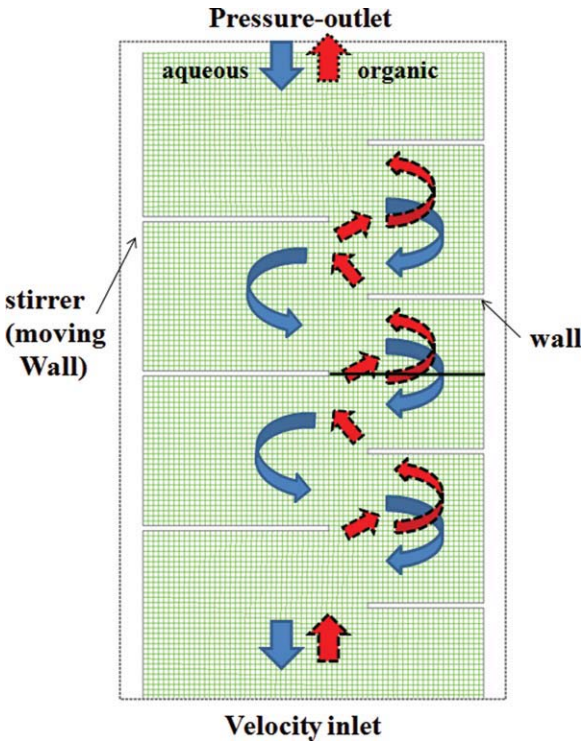

Figure 4. Computational grid.

[Color figure can be viewed in the online issue, which is available at wileyonlinelibrary.com.]

mass force and the lift force were neglected. For the evaluation of the drag coefficient, the model of Schiller and Naumann was applied.[28] In this connection, constant Sauter mean diameters were applied in the simulation, which were estimated by evaluating digital PIV photos from the experiments.

The computational model was a 2D axis-symmetric geometry consisted of 20,000 quadrilateral cells with 3-mm grid spacing (see Figure 4). For turbulence modeling, the standard k–ε, realizable k–ε turbulence models, and the Reynolds Stress model were applied together with standard wall functions. Details of the different turbulence models can be found in literature.[28] For the calculation of the multiphase turbulence, the Fluent mixture turbulence model was used, which is an extension of the single-phase model.[28] Velocity-inlet and pressure-outlet boundary conditions were applied at the top and bottom of the computational grid. The boundary condition for the single water phase is $v = 0.00175$ m/s resulting in 1000 L/h. For the two-phase flow, the boundary conditions are $v_{aq} = 0.000985$ m/s and $v_{org} = 0.0089$ m/s (10% volume fraction at the inlet). Values close to zero were given for the turbulent kinetic energy and the energy dissipation. QUICK differencing schemes were used to discretise the convection terms whereas PRESTO was used as the discretization method for pressure. The first-order implicit scheme was used for time advancing, and the pressure–velocity coupling was done using the PISO algorithm in single-phase and the SIMPLE algorithm in two-phase flow. A time step size between 0.001 and 0.01 s was chosen and more than 20 s was simulated (100 s in two-phase mode). Residuals below 10^{-5} were chosen as convergence criteria (10^{-4} for the two-phase flow). For the two-phase flow, the total volume of the dispersed phase was monitored till it become constant. The computational time for one time step is around 90 s using a single 3 GHz CPU and two-phase flow. The overall computing time for 10,000 time steps at a time step size of 0.01 s (100 s real time) is, therefore, 250 h.

Results and Discussion

Single-phase flow

CFD simulations have been performed with three turbulence models, namely the standard k–ε, realizable k–ε, and the RSM. PIV measurements have been conducted for the two different measurement areas shown in Figure 2. Different stirrer revolutions were investigated at a single-phase water flow rate of 1000 L/h. As only 2D PIV measurements were possible in the extractor, the velocities are compared with the PIV measurement plane. The velocity magnitude in the PIV measurement plane is calculated from the axial (x coordinate) and radial velocities (z coordinate). The swirl velocity (y coordinate) is not compared.

$$u = \sqrt{u_x^2 + u_z^2} \tag{9}$$

Zone 1, from the stirrer to the column wall, is the most interesting part of the compartment since it is the mixing

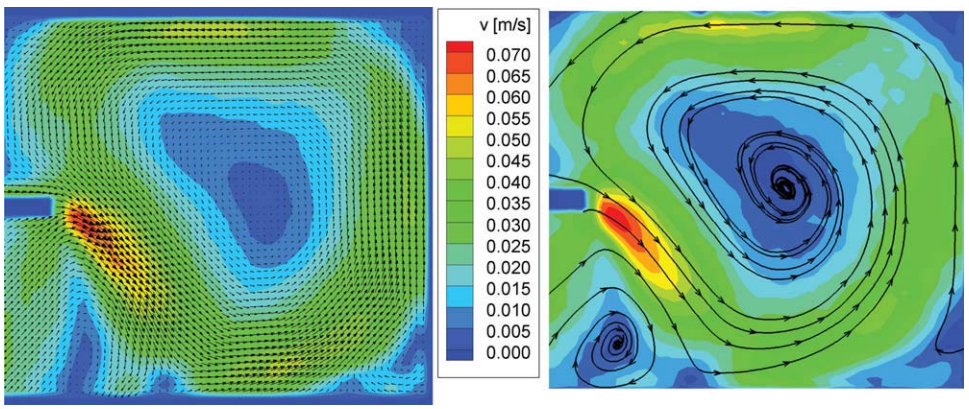

Figure 5. Single-phase PIV measurements, average velocity magnitude and vectors (left), streamtraces plot (right) Zone 1, $n_{stirrer}$ = 50 rpm.

[Color figure can be viewed in the online issue, which is available at wileyonlinelibrary.com.]

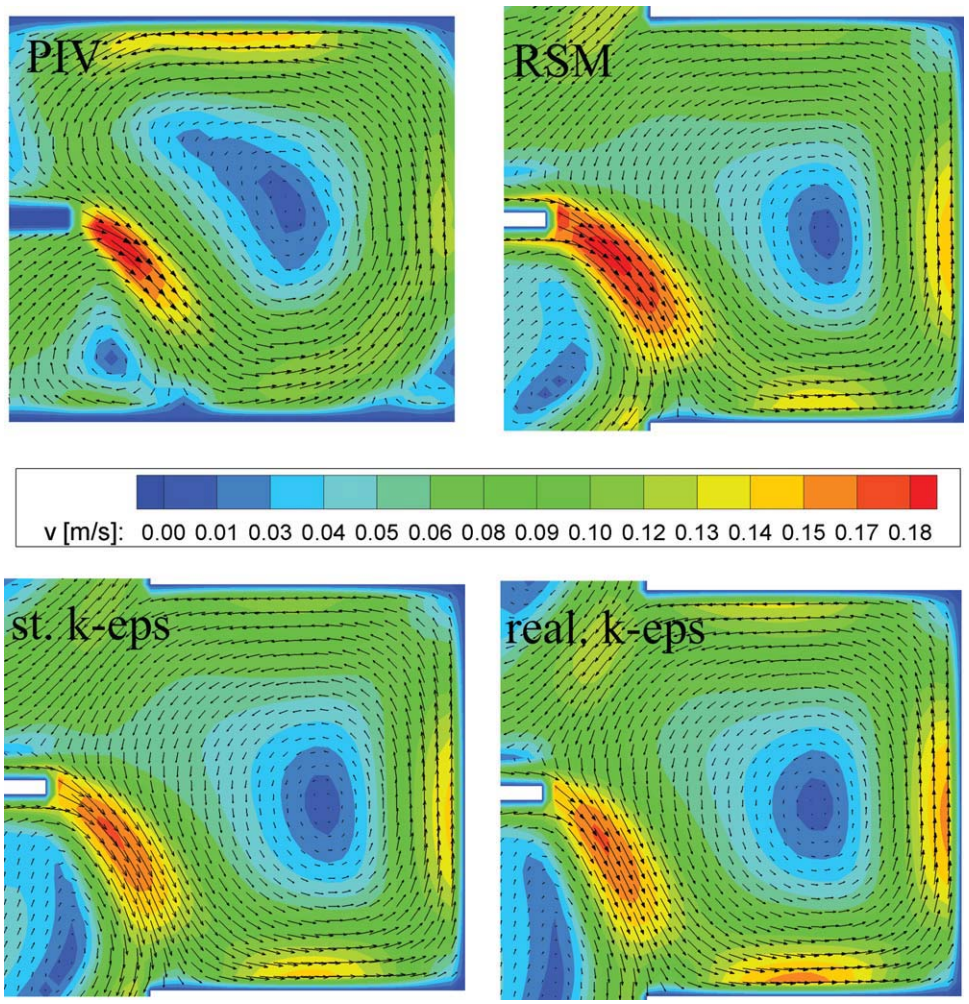

Figure 6. Comparison PIV-CFD, average velocity magnitude and vectors, Zone 1, $n_{stirrer}$ = 50 rpm.

[Color figure can be viewed in the online issue, which is available at wileyonlinelibrary.com.]

zone of the compartment with the highest energy dissipation. PIV contours of average velocity magnitude and velocity vectors of Zone 1 at 50 rpm are depicted in Figure 5. A qualitative comparison between the PIV measurements and the CFD simulations is visible in Figure 6. It can be seen that the CFD simulations are in good agreement with the simulations. As expected, the highest velocities are near the stirrer tip. From the velocity vectors and the contours, one big vortex can be estimated in the compartment between the stators. The PIV and CFD velocities are compared along a line at the stirrer level from the stirrer to the column wall. The velocities along this line are shown in Figure 7. The CFD predicted maximum velocity and the velocities at the stirrer level are predicted well by all turbulence models. Only minor discrepancies are visible for the shape of the vortex and the dead zone. The same graphs are shown for 150 rpm (Figures 8–10) and 300 rpm (Figures 11–13). For the higher stirrer speeds, the shape of the vortices and dead zone are almost identical but at a higher velocity magnitude. Again, all turbulence models can predict the fluid dynamics and the shape of the vortex at 150 rpm (Figures 9 and 10). At 300 rpm, the standard k–ε fails to predict the shape of the vortex and the maximum velocities (Figures 12 and 13). These results can confirm previous work, where the realizable k–ε model and the RSM were best for single-phase flow in a RDC 150 mm pilot plant column,[12] whereas the standard k–ε model could also not meet this accuracy.[12,20] CFD

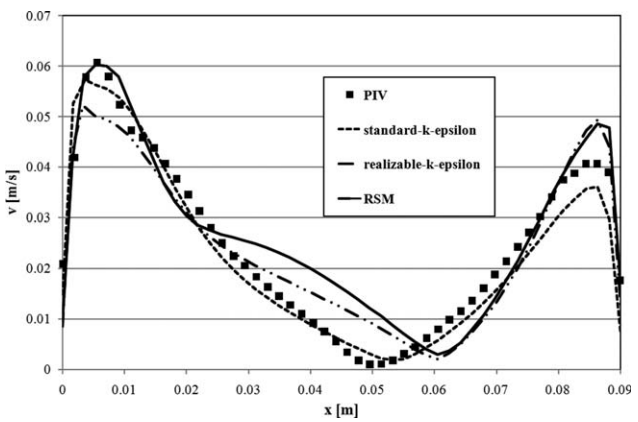

Figure 7. Comparison PIV-CFD, single-phase measured and calculated average velocity magnitude at stirrer level, Zone 1, $n_{stirrer}$ = 50 rpm.

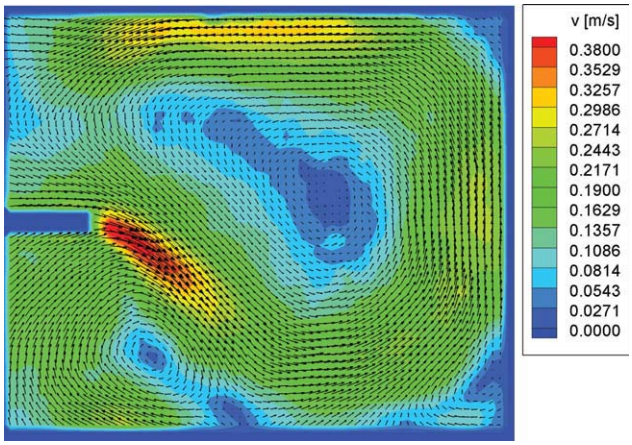

Figure 8. Single-phase PIV measurements, average velocity magnitude and vectors, Zone 1, $n_{stirrer}$ = 150 rpm.

[Color figure can be viewed in the online issue, which is available at wileyonlinelibrary.com.]

can predict the one-phase flow field in the industrial scale RDC extractor exactly, whereas all flow phenomena such as vortices and dead zones can be described. Grid independency was assured by applying a 1 mm grid, which gave the same results at much higher computational load.

Local turbulent energy dissipation

The turbulent energy dissipation was calculated within the framework of PIV analysis from Eq. 3. Different stirrer speeds, 100, 200, and 300 rpm for a water flow rate of 1000 L/h were investigated. The stirrer Reynolds number range is between 75,000 and 4×10^5. It depends on the rotation per second N, the stirrer diameter D_r, the density ρ_c, and the dynamic viscosity η_c.[29]

$$Re = \frac{D_r^2 N \rho_c}{\eta_c} \tag{10}$$

The transition from laminar to turbulent flow in the compartment is expected for a Reynolds number $Re > 6 \times 10^4$.[29]

The spatial resolution of the PIV measurements affects the magnitude of the measured dissipation rate. To fully resolve

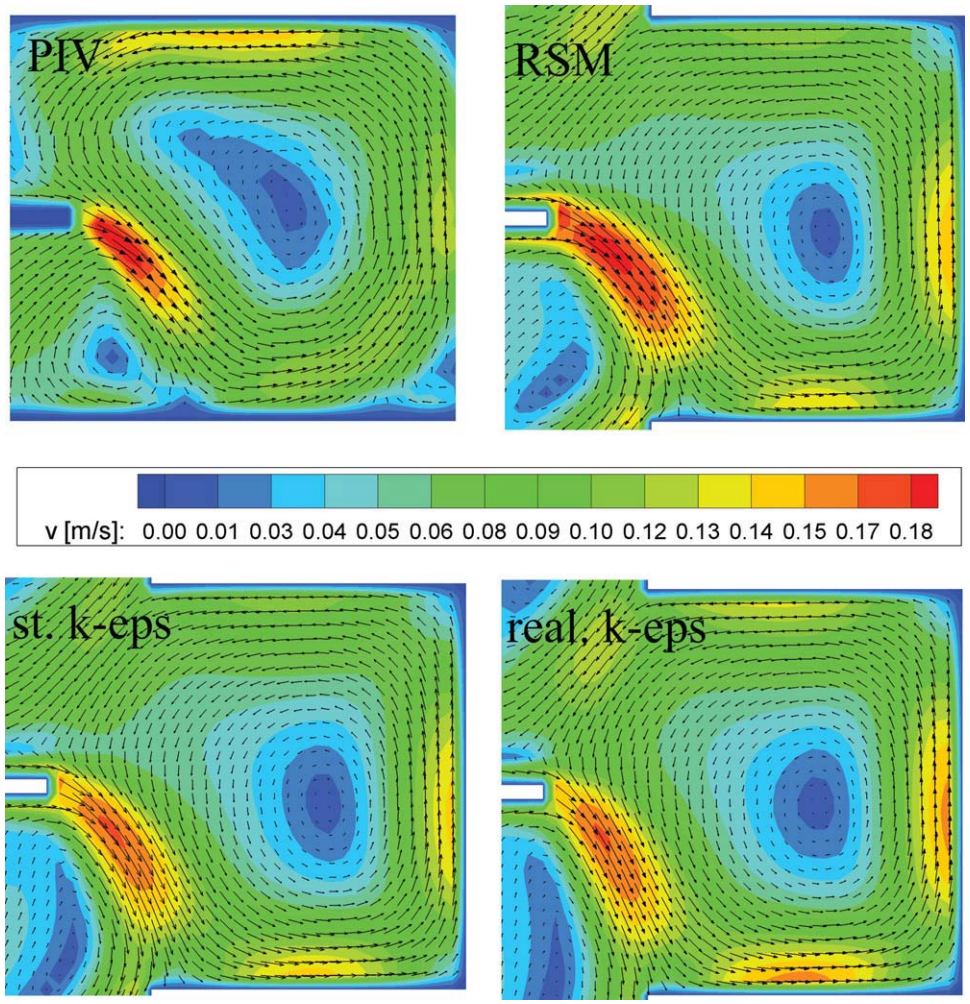

Figure 9. Comparison PIV-CFD, average velocity magnitude and vectors, Zone 1, $n_{stirrer}$ = 150 rpm.

[Color figure can be viewed in the online issue, which is available at wileyonlinelibrary.com.]

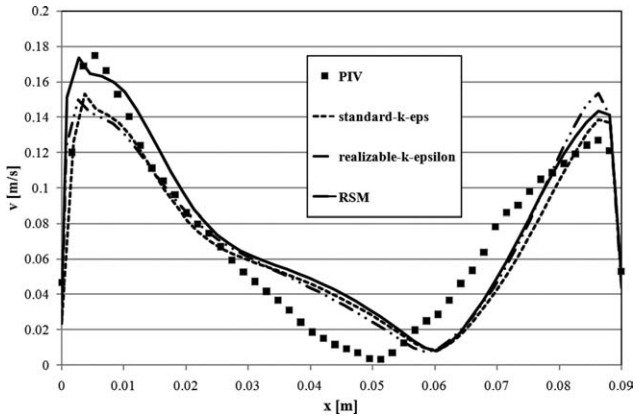

Figure 10. Comparison PIV-CFD, single-phase measured and calculated average velocity magnitude at stirrer level, Zone 1, $n_{stirrer}$ = 150 rpm.

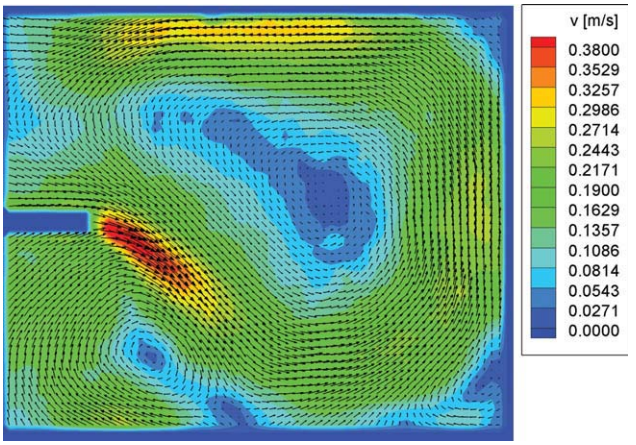

Figure 11. Comparison PIV-CFD, average velocity magnitude and vectors, Zone 1, $n_{stirrer}$ = 300 rpm.

[Color figure can be viewed in the online issue, which is available at wileyonlinelibrary.com.]

the spatial behavior of the turbulence quantities of a turbulent flow field, it is necessary to measure down to the Kolmogorov length scale. Saarenrinne et al.[27] have shown the turbulent kinetic energy and the dissipation rate spectrums from Helland's theoretical spectrum. From these spectrums it can be seen that to reach 90% of the dissipation rate, the spatial resolution Δ should be around 2η, and to reach 65% 9η. On the other hand, to reach 65% of the turbulent kinetic

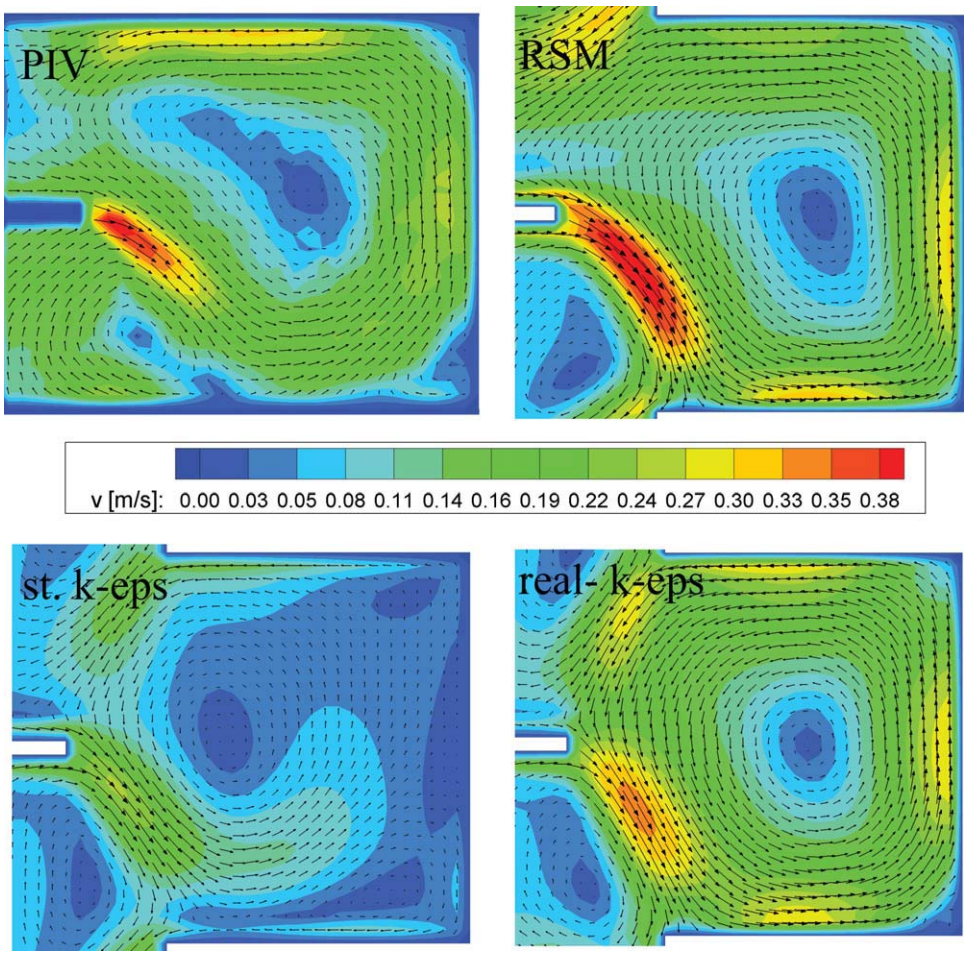

Figure 12. Comparison PIV-CFD, average velocity magnitude and vectors, Zone 1, $n_{stirrer}$ = 300 rpm.

[Color figure can be viewed in the online issue, which is available at wileyonlinelibrary.com.]

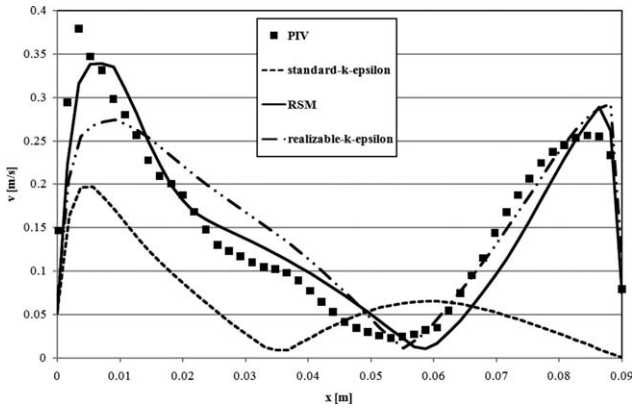

Figure 13. Comparison PIV-CFD, single-phase measured and calculated average velocity magnitude at stirrer level, Zone 1, $n_{stirrer}$ = 300 rpm.

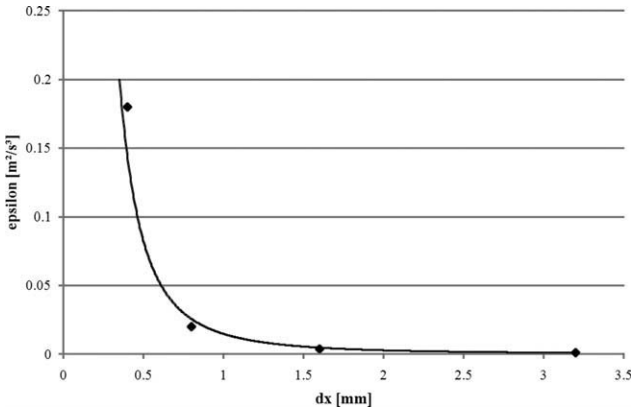

Figure 14. Influence of the spatial resolution on the measured maximum turbulent energy dissipation in PIV.

energy the spatial resolution should be only around 90η, and to reach 65% around 20η.[27] Because of the huge compartment area in the industrial scale RDC ($area_{compartment}$ = 35,640 mm^2), a small measurement zone (see Figure 2, Zone 2) at the stirrer was chosen, to increase the spatial resolution. This zone is also of main interest, since the main energy input is at the stirrer and the stirrer tip. In practice, the droplets break in this region at the stirrer wall or in the stirrer outflow. A correct prediction of the turbulent energy dissipation in CFD is crucial for a correct modeling of the breakage and coalescence phenomena and a coupling with PBMs.[19] That's why the measured PIV energy dissipation was compared to the CFD predictions to investigate the predictivity of CFD for the turbulence characteristics. A calculation of the energy dissipation for the whole compartment from the single-phase velocity measurements (see above) did not deliver reliable results because of the lower resolution and the resulting high uncertainties.

The PIV spatial resolution for the different interrogation areas (64 × 64 px^2, 32 × 32 px^2, and 16 × 16 px^2) and the measurement zone is shown in Table 2. The maximum measured energy dissipation for 100 rpm as a function of these spatial resolutions is depicted in Figure 14. From this figure, it becomes clear, that the smaller measurement Zone 2 around the stirrer was necessary to reach a lower spatial resolution together with 16 × 16 pixels interrogation areas.

In Table 3, the maximum and average values for the energy dissipation and the corresponding Kolmogorov length scales (Eq. 5) at 100 rpm for PIV and CFD are presented. The average values were calculated by means of an area integral over the whole zone. From this table it can be seen that the spatial resolution is around five times the Kolmogorov length scale η for the average energy dissipation. For the maximum value of the energy dissipation only 10η are reached. Therefore, it was assumed that only around 65% of the energy dissipation was measured and the values were scaled in Tecplot by a factor 1.55. The scaled values are also shown in Table 3 and agree well with the average values predicted by CFD. The different turbulence models predict almost identical results for the energy dissipation (see Table 3 and Figure 15).

The contours of the energy dissipation in PIV, unscaled (top) and scaled (bottom), are depicted in Figure 16 and compared to CFD results. It is visible that the scaled energy dissipation in the stirrer outflow agrees well with the CFD results. The maximum values in CFD are higher than the maximum PIV values. The same is also visible in Figures 17 and 18, where the scaled energy dissipation is compared along the stirrer level from the stirrer to the column wall. Figure 17 compares the values close to the stirrer wall, where the PIV measurements were carried out and high values for the energy dissipation are visible. Because of non-idealities and small oscillations of the stirrer in the experiments, it is not possible to measure exactly close to the stirrer wall. This explains the lower measured values close to the stirrer. The higher values in CFD close to the wall can, therefore, neither be negated nor confirmed from the measurement. At least, the CFD predicted energy dissipation near the stirrer is in the same order of magnitude and seems reasonable based on the slope. In literature, CFD is known to underpredict the dissipation (e.g., as shown in Ref. 14), which is not the case here. Note that the small investigated zone is in the near wall regions, which is influenced by the wall effect and the applied wall function.

The CFD predicted energy dissipation near the stirrer is dependent on the grid near the wall and the wall functions. In

Table 2. PIV Measurements Spatial Resolutions

Measurement Area	PIV Resolution (px^2)	Spatial Resolution (mm)
1	32	3.39
8100 mm^2	16	1.69
	8	0.85
3	32	1.60
1500 mm^2	16	0.80
	8	0.40

Table 3. CFD and PIV Maximum and Average Values for ε and the Corresponding Kolmogorov Length Scales, 100 rpm

	Turbulent Energy Dissipation ε (m^2/s^3)		Kolmogorov Length Scale η (mm)	
100 rpm	Maximum Value	Average Value	Minimum	Average
PIV	0.19	0.0214	0.0425	0.083
Standard *k–ε*	0.64	0.0351	0.0347	0.073
Realizable *k–ε*	0.63	0.0342	0.0356	0.074
RSM	0.69	0.0390	0.0353	0.071
PIV scaled	0.38	0.0328	0.0433	0.074

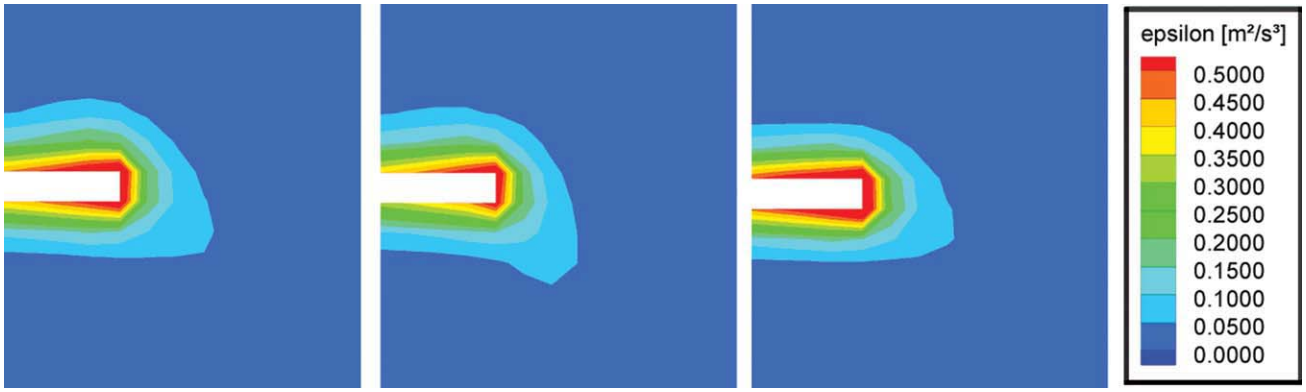

Figure 15. CFD, turbulent energy dissipation at 100 rpm, standard *k*–ε, realizable *k*–ε, RSM (left to right).

this work, the standard wall functions were applied without giving closer attention to this aspect, since it is also not possible to compare the near wall values to experimental PIV data. The y^+ values are around 30 and near the optimum.[28] A finer grid (e.g., 1 mm) would not be suitable for the near wall regions using the standard wall functions since the wall unit would be far below 30. Some test simulations were also carried out with an enhanced wall treatment applying a fine near wall grid. For the RDC extractor, the grid becomes very fine near the stirrer wall to reach y^+ values around 1. There is a dramatic increase in computational time and no improvement for the velocities. On the other hand, at the vertex of the stirrer even higher values for the energy dissipation were predicted.

In Figure 18, the energy dissipation is compared in the core flow afar from the wall (see x coordinate). Only a few PIV measurements are available leftmost for this region. In this region, the energy dissipation is one to a few orders of magnitude smaller than near the stirrer. The different turbulent models predict similar results for this region around the dead zone.

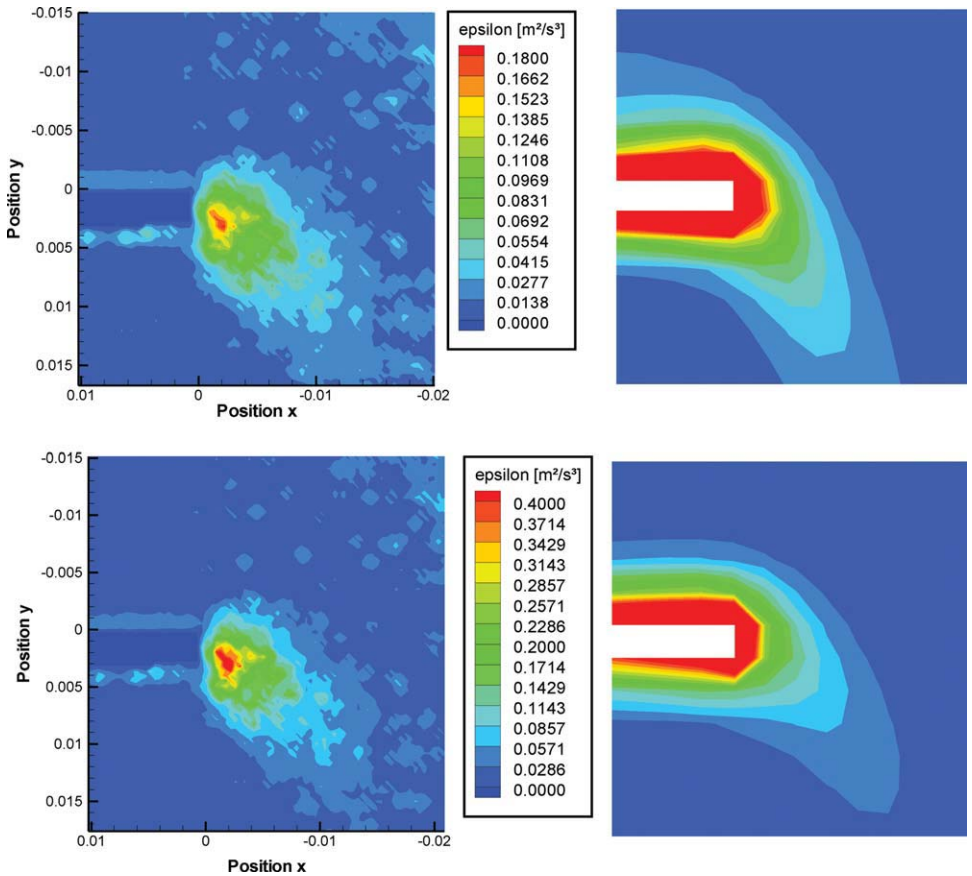

Figure 16. Turbulent energy dissipation at 100 rpm.

Top: PIV 8 × 8 px^2 (left), Fluent (right). Bottom: Scaled energy dissipation in PIV based on Kolmogorov length scale analysis 8 × 8 px^2 (left), Fluent realizable *k*–ε (right).

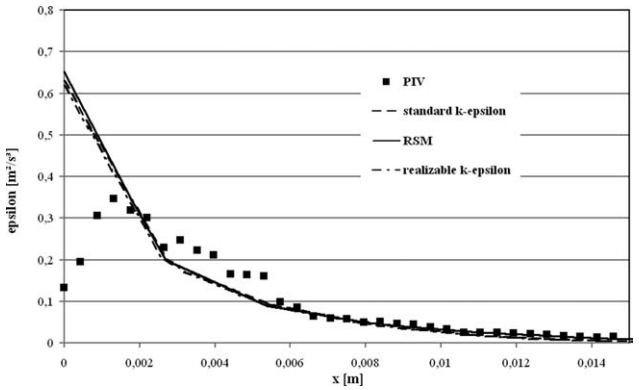

Figure 17. Comparison turbulent energy dissipation at 100 rpm at the stirrer level, PIV 8 × 8 px² (scaled), *x* coordinate distance from the stirrer to the wall.

The situation of the energy dissipation is worse for 200 and 300 rpm. The measured energy dissipation (Zone 2) at 200 and 300 rpm and the corresponding Kolmogorov length scales are given in Table 4. The spatial resolution is now only around 10η for the area average value and around 20η for the maximum values. A scaling based on the rules of thumb of Saarenrinne et al.[26] is now hardly possible. Alekssenko et al.[26] proposed an underestimation coefficient f_ε based on Pao's spectrum:

$$f_c = 1 - \exp\left(-\frac{3}{2}\alpha\left(\frac{\pi\eta}{\Delta}\right)^{4/3}\right) \tag{11}$$

where the parameter $\alpha = 1.6$. The same authors also developed a fit function to scale the measured values. The fit function reported by Alekseenko et al.[26] is:

$$f_\varepsilon = 1 - \exp\left(-\alpha\left(\frac{3}{2}\left(\frac{\pi\eta}{\Delta}\right)^{4/3} + \left(\frac{\pi\eta}{\Delta - 5.87\eta}\right)^{3.15}\right)\right) \tag{12}$$

where $\Delta > 5.87\eta$. The underestimation coefficients of the turbulent energy dissipation based on Pao's spectrum and the fit function by Alekseenko et al.[26] are shown in Figure 20. Both correlations were applied to scale the measured values of the energy dissipation. For

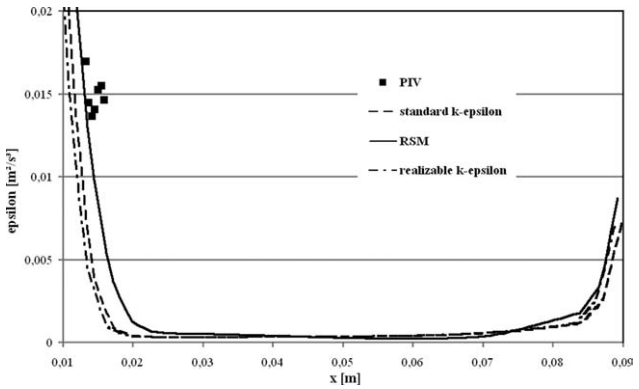

Figure 18. Comparison turbulent energy dissipation at 100 rpm at the stirrer level (core flow), PIV 8 × 8 px² (scaled), *x* coordinate distance from the stirrer to the wall.

Table 4. CFD and PIV Maximum and Average Values for ε at 200 and 300 rpm, PIV Measurements Scaled with Fit Functions (Figure 20)

	Turbulent Energy Dissipation ε (m^2/s^3)		Kolmogorov Length Scale η (mm)	
	Maximum Value	Average Value	Minimum	Average
200 rpm				
PIV measured	0.66	0.075	0.0351	0.0604
PIV scaled max	2.2	0.251	0.0260	0.0447
PIV scaled local	2.2	0.091	0.0260	0.0576
PIV scaled Pao	2.07	0.135	0.0273	0.0522
Standard k–ε	3.4	0.18	0.0233	0.0485
Realizable k–ε	3.65	0.199	0.0229	0.0473
RSM	3.7	0.202	0.0228	0.0472
300 rpm				
PIV measured	1.2	0.276	0.0302	0.0436
PIV scaled max	6.01	1.379	0.0202	0.0292
PIV scaled local	6.01	0.512	0.0202	0.0374
PIV scaled Pao	6.1	0.588	0.0226	0.0361
Standard k–ε	9.2	0.526	0.0182	0.0371
Realizable k–ε	10.5	0.623	0.0176	0.0356
RSM	11.5	0.608	0.0172	0.0358

the fit function, the value of the true energy dissipation was found in the following iterative way. At the first stage, f_ε was taken to be equal to unity and approximate value of η was found from $\eta = (\nu^3 f_\varepsilon/\varepsilon_{meas})^{1/4}$. At the next step, f_ε was estimated from Eq. 11 and then η was recalculated. About five iterations are enough for a good convergence.[26] The scaled values for the energy dissipation are also shown in Table 4. Alekseenko et al. have taken the maximum value of ε in the measurement zone as a constant ε_{meas}. These values are named "PIV scaled max" in Table 4 and the average value for ε is too high, since the values of f_ε are too small in the outer regions. In the next case, the local values of ε were taken as ε_{meas} to have an individual scaling parameter ("PIV scaled local" in Table 4). Here, the resulting average value becomes smaller than the average in CFD (Table 4). Note that the fit function does not scale values where $\Delta < 5.87\eta$. By applying the fit function, there is no scaling in the outer regions with a satisfying spatial resolution ($\Delta < 5.87\eta$). Finally, f_ε was taken directly from Pao's spectrum in Figure 19 for

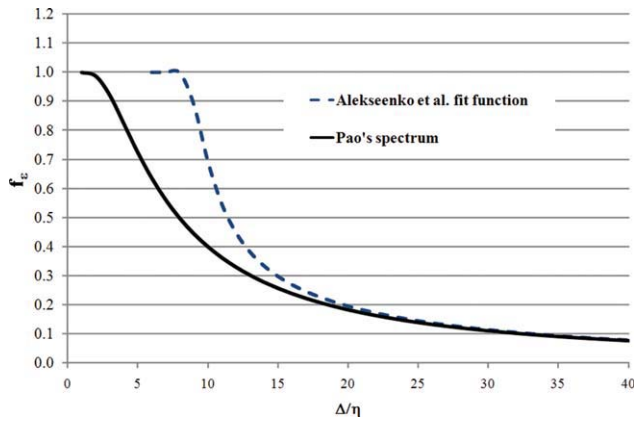

Figure 19. Influence of the spatial resolution in PIV on the underestimation coefficient of the turbulent energy dissipation, Pao's spectrum, and fit function by Alekssenko et al.

[Color figure can be viewed in the online issue, which is available at wileyonlinelibrary.com.]

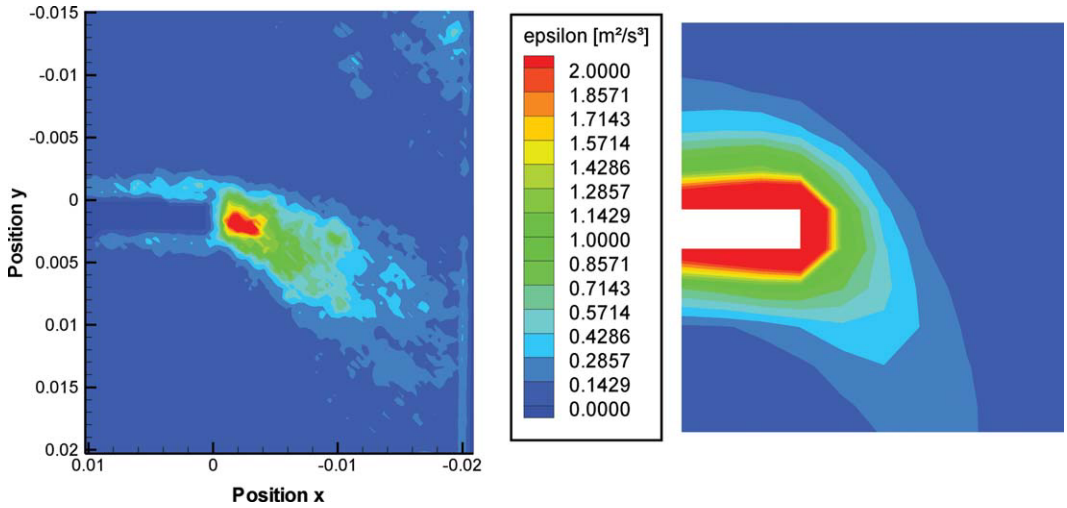

Figure 20. Turbulent energy dissipation at 200 rpm, scaled energy dissipation in PIV (fit function), PIV 8 × 8 px^2 (left), Fluent (realizable k–ε) (right).

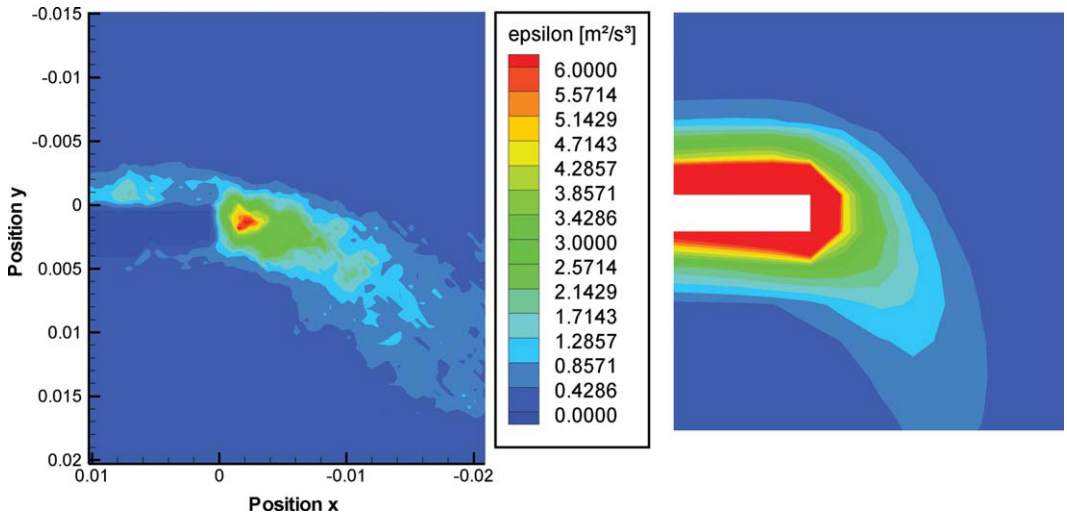

Figure 21. Turbulent energy dissipation at 300 rpm, scaled energy dissipation in PIV (fit function), PIV 8 × 8 px^2 (left), Fluent (realizable k–ε) (right).

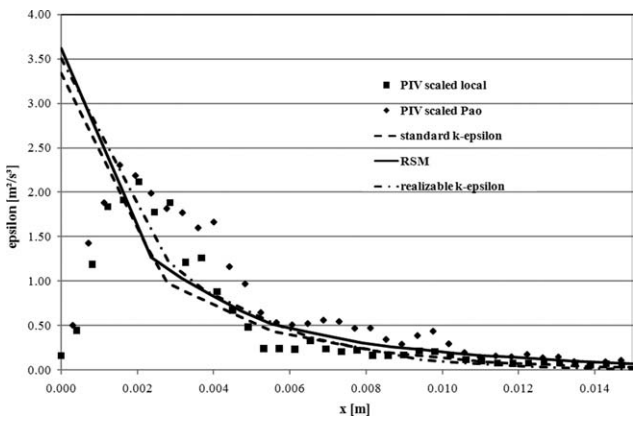

Figure 22. Comparison turbulent energy dissipation at 200 rpm at the stirrer level, PIV 8 × 8 px^2 (scaled) and CFD, x coordinate distance from the stirrer to the wall.

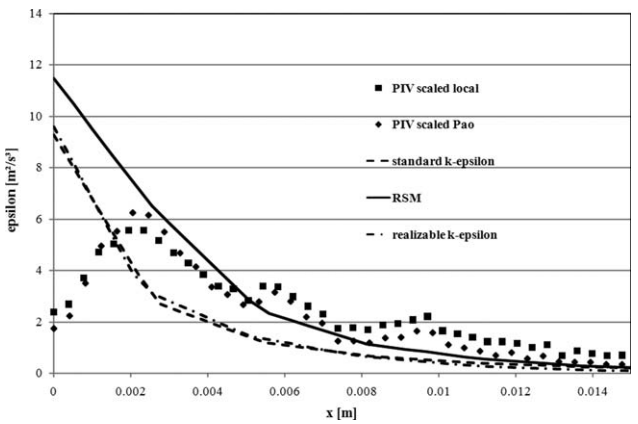

Figure 23. Comparison turbulent energy dissipation at 300 rpm at the stirrer level, PIV 8 × 8 px^2 (scaled) and CFD, x coordinate distance from the stirrer to the wall.

Table 5. CFD Mean Turbulent Energy Dissipation for the Whole Compartment, Comparison to Correlation by Kosters Eq. 14

	Volume-Average Energy Dissipation	
	100 rpm	300 rpm
Standard k–ε	0.00813	0.1306
Realizable k–ε	0.0087	0.133
RSM	0.014	0.210
Correlation Eq. 14, ($d_r = 0.27$ m)	0.0145	0.32
Correlation Eq. 14, ($d_r = 0.25$ m)	0.0088	0.24

the local values of ε as ε_{meas} ("PIV scaled Pao" in Table 4). The average value for ε is now higher than the scaled one with the fit function but still lower than the average value in CFD. The maximum value in CFD is always higher than in PIV as discussed above. The good news is that the average value in CFD lies between both underestimation coefficients methods and is in the same order of magnitude. For a bigger measurement area, the deviations would be much less since the Kolmogorov length scale is fully resolved in the outer regions of the compartment.

The scaled turbulent energy dissipation with the fit function is compared to the CFD results in Figure 20 (200 rpm) and Figure 21 (300 rpm). Both methods give the same qualitative and quantitative distribution in the stirrer outflow. The results show that a scaling is possible at higher stirrer speeds but remains difficult especially when the Kolmogorov length scale is only partially resolved ($\Delta > 10\eta$). In Figures 22 and 23, the scaled PIV values are plotted at the stirrer level and compared to the CFD results. There is a good agreement for the distance $0.002 < \times < 0.014$ m to the stirrer. The RSM delivers the best results especially at 300 rpm. As discussed before, the values close to the stirrer tip (2 mm) cannot be compared. All things considered, the CFD results are in good agreement to the scaled PIV measurements although both suffer from uncertainties at the industrial scale and the high energy input.

The huge compartment area in the RDC450 does not allow the estimation of the turbulent energy dissipation or dissipation integral for the whole compartment. For the sake of completeness, the dissipation integrals from CFD are compared to a correlation for the power input in an RDC compartment proposed by Kosters[21]:

$$P = N_p \rho_c N^3 D_r^5 \tag{13}$$

For a comparison with CFD, the mean dissipation can be easily calculated as follows:

$$\bar{\varepsilon} = \frac{P}{\rho_c V_{comp}} \tag{14}$$

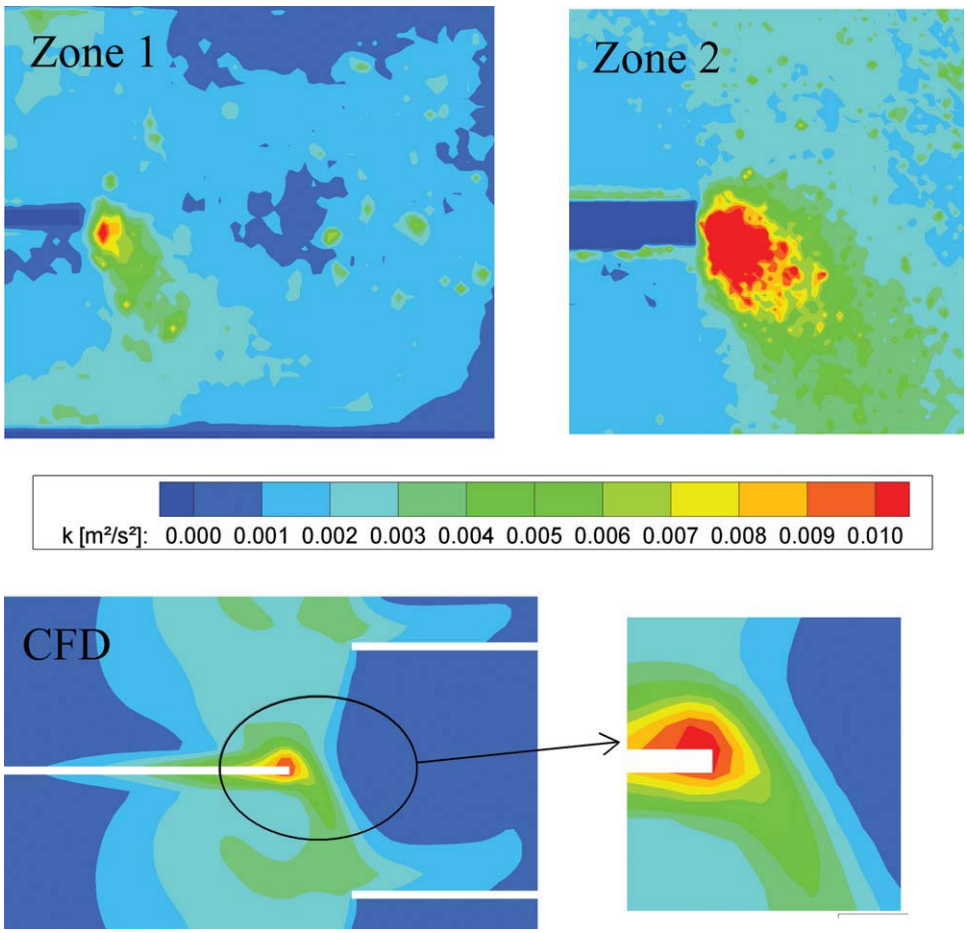

Figure 24. Turbulent energy *k* at 100 rpm.

Top: PIV, 16 × 16 px^2 (left), 8 × 8 px^2 (right). Bottom: Fluent turbulent energy k, standard k–ε model.

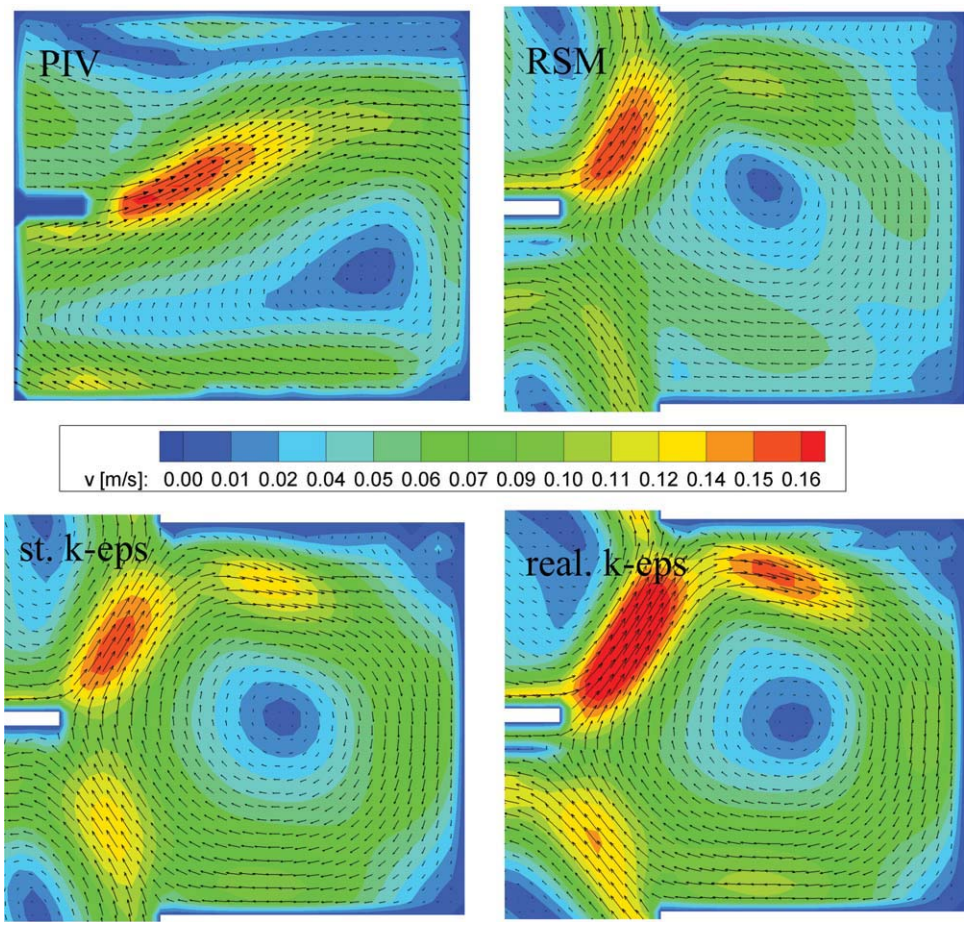

Figure 25. Comparison PIV-CFD, two-phase average velocity magnitude and vectors in aqueous phase, Zone 1, $n_{stirrer}$ = 100 rpm.

[Color figure can be viewed in the online issue, which is available at wileyonlinelibrary.com.]

The average energy dissipation by Eq. 14 ranges from 0.01 m^2/s^3 (100 rpm) to 0.32 m^2/s^3 at 300 rpm with an impeller power number of 0.3 for the RDC. The predicted mean energy dissipation values from CFD are shown in Table 5 and compared to the results of Eq. 14. The CFD predicted values are now lower. Now for the whole compartment, the effects of the wall functions are small in comparison to the core flow. It is known that the k–ε models underpredict the turbulent properties in stirred tanks or columns.[14] On the other hand, it is questionable if the correlation Eq. 13 can exactly describe the energy input of the RDC at this huge diameter. A stirrer diameter of 0.25 m instead of the present 0.27 m would result in 0.24 m^2/s^3 mean dissipation value and, therefore, in some uncertainties in the correlation (Table 5).

Turbulent kinetic energy

Results for the turbulent kinetic energy k in the two PIV measurement zones are depicted in the upper part of Figure 24 and compared to the CFD results (bottom Figure 24). As expected, the turbulent kinetic energy can be easily resolved and does not need high resolutions as for the calculation of the dissipation. In contrast to the energy dissipation, results for the turbulent kinetic energy k seems to be independent of the spatial resolution and contours for both zones (left: Zone 1, right: Zone 2) are almost identical and also agree well with the CFD results. For the maximum values of the kinetic energy around 20η are reached for Zone 1 and around 10η are reached for the smaller Zone 2. The negligible influence of the resolution in this region (resolution below 20η) can confirm the work of Saarenrinne et al.[26]

Recapiulatory, the turbulent kinetic energy is 100% resolved for the RDC 450, while the turbulent energy dissipation can easily be scaled at 100 rpm. A scaling for the energy dissipation at higher stirrer speed is also possible.

Two-phase flow

The two-phase flow was investigated at 100 and 300 rpm at volume flow rates of 500 L/h per phase.

The iso-optical system allows the measurement of the velocities in the aqueous phase. Besides the PIV measurements, again all turbulence models were varied in CFD. The velocity fields of the continuous water phase both for CFD simulation and PIV measurements are depicted in Figure 25 (100 rpm) and Figure 26 (300 rpm). As in the single-phase flow, one big vortex can be estimated in the compartment between the stators. The vortex shift or turn around now because of the rising droplets. The same behavior was already observed in the pilot plant column.[12] All turbulence models can predict the vortex and the dead zones. However, the vortex in PIV is smaller and compressed and therewith

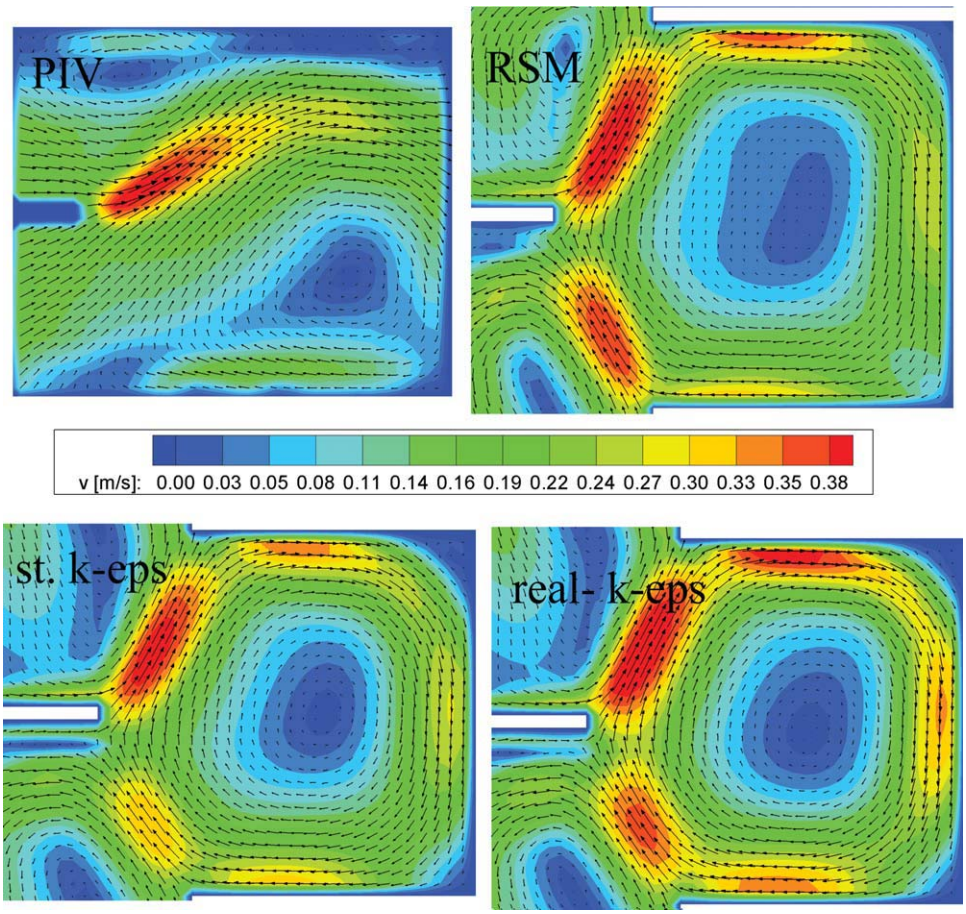

Figure 26. Comparison PIV-CFD, two-phase average velocity magnitude and vectors in aqueous phase, Zone 1, $n_{stirrer}$ = 300 rpm.

the dead zone is also shifted. The velocities at 100 and 300 rpm are compared along a line at the stirrer level from the stirrer to the column wall in Figures 27 and 28. In contrast to the single-phase flow, the deviations are now higher because of the different location of the dead zones and the different shape of the vortices. All turbulence models predict almost identical results at 100 and 300 rpm. Nevertheless, the maximum velocities and the qualitative velocity distribution in the compartment are predicted well. It has to be pointed out that especially the velocities in the 2D PIV measurement area are hard to predict since they are only results

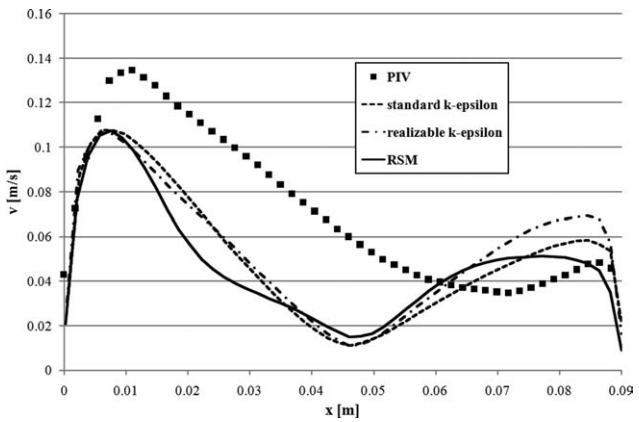

Figure 27. Comparison PIV-CFD, two-phase measured and calculated average velocity magnitude in aqueous phase at stirrer level, Zone 1, $n_{stirrer}$ = 100 rpm.

[Color figure can be viewed in the online issue, which is available at wileyonlinelibrary.com.]

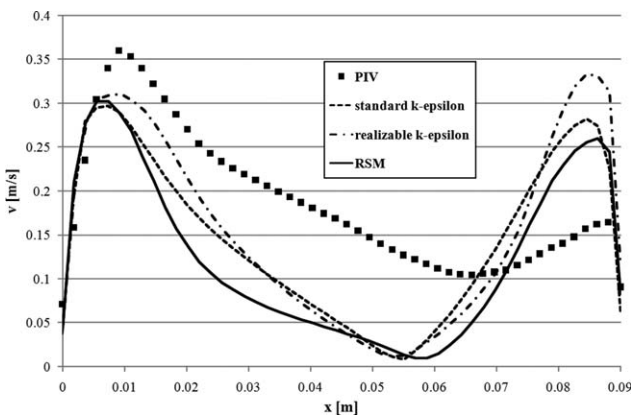

Figure 28. Comparison PIV-CFD, two-phase measured and calculated average velocity magnitude in aqueous phase at stirrer level, Zone 1, $n_{stirrer}$ = 300 rpm.

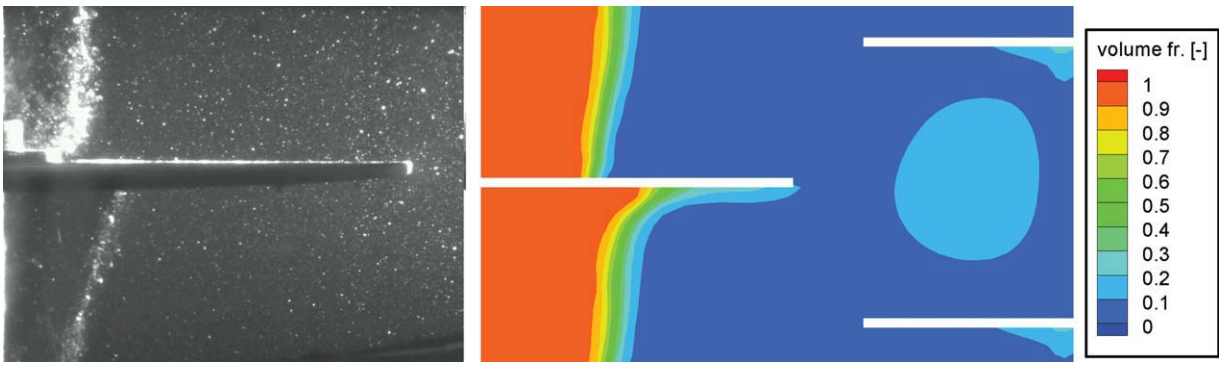

Figure 29. Swirl near shaft at 300 rpm, PIV picture (left), CFD volume fraction dispersed phase (realizable *k*–ε) (right).

[Color figure can be viewed in the online issue, which is available at wileyonlinelibrary.com.]

of the shear stresses while the main velocity is the swirl velocity normal to the *xz*-plane.

In Figures 25 and 27, the volume fraction in CFD under the stators is smaller than in PIV, which becomes obvious from the velocity vectors in the aqueous phase. It was also noticed that a swirl of dispersed phase developed at 300 rpm at the shaft during the PIV measurements. This phenomenon is depicted in Figure 29 and compared to the volume fraction in of the dispersed phase in CFD. The same swirl of dispersed phase is predicted in CFD and it is also visible that the droplets do not accumulate under the stators and are dispersed in the compartment. However, a more profound investigation for the volume fraction was not possible in PIV. Finally, the average velocity magnitude and vectors of the whole compartment from CFD are depicted in Figure 30. It is visible that the velocities at the left side of the compartment, near to the shaft are very small. This can also explain the accumulation of the dispersed phase near the shaft. The layout rule of Kosters[21] for the shaft would result in a bigger diameter and would probably avoid this effect. As described before, the diameter of the shaft was held constant for the scale-up to avoid a 160 mm shaft.

The differences between PIV and CFD could be explained by the smaller volume fraction under the stators in CFD. As the droplet diameters were only estimated from the digital photos in the laser measurements and are hard to identify, bigger and smaller diameters in the range of 0.5–4 mm were also tested in the CFD simulations but did not result in an improvement. The present two-phase model uses a constant Sauter mean diameter and cannot account for coalescence and an accumulation of the droplets under the stators. A coupled CFD-PBM model which can describe the breakage near the stirrer and the coalescence under the stators can describe the local drop size in one compartment and could probably predict better results for the shape of the vortex. In addition, it is well-known that the multiphase models still demand improvement. As expected, the overall prediction of the velocity fields in the RDC450 is reasonable but worse than in the smaller RDC150 pilot plant column in previous work.[12]

Conclusions

Single-phase and two-phase simulations of a RDC extractor at industrial scale were carried out and compared to 2D PIV measurements. Different turbulence models were applied in the CFD simulations. The results show that CFD can predict the one-phase flow field in the industrial scale RDC extractor exactly, whereas all flow phenomena such as vortices and dead zones can be described. The turbulent energy dissipation was estimated from single-phase PIV measurements and compared to the results of the CFD simulations. The influence of the spatial resolution in PIV on the measured energy dissipation was analyzed. Different methods based on a Kolmogorov length scale analysis were applied to scale the local measured energy dissipation. The scaled energy dissipation derived from PIV measurements agree quite well with the CFD results but remains challenging at higher stirrer speeds. CFD can predict the energy dissipation in the stirrer outflow, whereas no comparison was available directly at the stirrer. A good agreement is reached

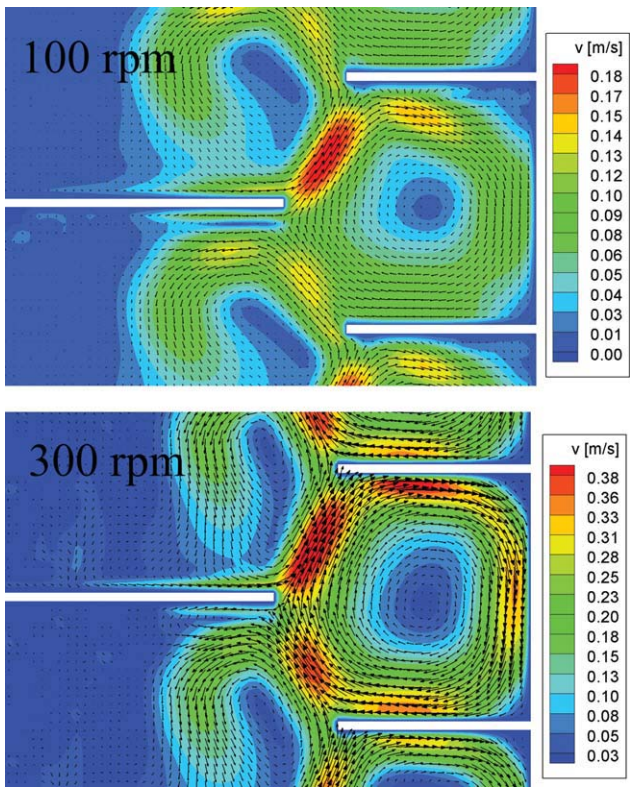

Figure 30. Two-phase CFD simulation, average velocity magnitude and vectors in aqueous phase in compartment at 100 and 300 rpm, realizable *k*–ε.

[Color figure can be viewed in the online issue, which is available at wileyonlinelibrary.com.]

for the average value, when the energy dissipation is scaled based on Kolmogorov length scale analysis.

For the two-phase flow, CFD fails to predict correctly the shape of the vortices and location of the dead zones, which are both shifted in CFD. Nevertheless, the predicted velocities and the qualitative velocity distribution in CFD are in good agreement with the experimental ones. The work shows, that CFD can predict hydrodynamic characteristics in an industrial scale RDC, but is still subject to improvements.

Acknowledgments

The authors acknowledge the financial support from the Deutsche Forschungsgemeinschaft (DFG).

Notation

D_r = disc diameter (m)
F = interaction force (N)
f_ε = underestimation coefficient
g = gravity constant (m/s^2)
k = turbulent kinetic energy (m^2/s^2)
n = stirrer revolutions (rpm)
N = stirrer revolution (s^{-1})
N_p = impeller power number
P = power input (kg/m^2/s^3)
t = time (s)
u = instantaneous velocity (m/s)
u' = local fluctuating velocity (m/s)
$\tilde{u}$ = root-mean-square velocity (m/s)
$\overline{u}$ = mean velocities (m/s)
V_{comp} = volume of an extraction compartment (m^3)
x = coordinate (m)
y^+ = dimensionless wall distance

Greek letters

α = volume fraction
Δ = spatial resolution (m)
ε = energy dissipation (m^2/s^3)
η = Kolmogorov length scale (m)
η_c = dynamic viscosity continuous phase (kg/s/m)
υ = kinematic viscosity (m^2/s)
ρ = density (kg/m^3)
ρ_c = density continuous phase (kg/m^3)
τ = stress–strain tensor (N/m^2)

Abbreviations

CFD = computational fluid dynamics
LDA = laser Doppler anenometry
LDV = laser Doppler velocimetry
PIV = particle image velocimetry
RDC = rotating disc contactor
rpm = revolutions per minute
RSM = Reynolds stress mod

Literature Cited

1. Erwin DL. *Liquid–Liquid Extraction. Industrial Chemical Process Design*. New York: McGraw-Hill, 2004.
2. Robbins LA, Cusack RW. Liquid–liquid extraction operations and equipment. In: Perry RH, Green DW, Maloney JO, editors. *Perry's Chemical Engineers' Handbook*, 7th Ed. New York: McGraw-Hill, 1997.
3. Mukhopadhyay A, Devulapalli B, Dutta A, Grald EW. Computational fluid dynamics: a virtual prototyping tool for materials engineering. *JOM*. 2004;56:44–48.
4. Fei WY, Wang YD, Wan YK. Physical modeling and numerical simulation of velocity fields in rotating disc contactor via CFD simulation and LDV measurements. *Chem Eng J*. 2000;78:131–139.
5. Haderer T, Marr R, Martens S, Siebenhofer M. Bestimmung auslegungsrelevanter hydrodynamischer Kenngrößen einer RDC-Extraktionskolonne mit CFD. *Chem Ing Tech*. 2005;77:1055.
6. Modes G, Bart H-J. CFD simulation of nonideal dispersed phase flow in stirred extraction columns. *Chem Eng Technol*. 2001;24:1242–1245.
7. Kolb P, Bart H-J, Fischer L. Entwicklung einer Miniplant-Extraktionskolonne. *Chem Eng Technol*. 2002;74:243–247.
8. You X, Bart H-J. Comparison of the Reynolds-averaged turbulence models on single phase flow simulation in agitated extraction columns. *Chin J Chem Eng*. 2003;11:362–366.
9. Gurker T, Haderer T, Marr R. CFD supported design in liquid–liquid extraction. In: Moyer BM, editor. Proceedings of the International Solvent Extraction Conference ISEC 2008. Montreal, Canada: Canadian Institute of Mining, Metallurgy and Petroleum, 2008:403–408.
10. Rieger R, Weiss C, Wigley G, Bart H-J, Marr R. Investigating the process of liquid–liquid extraction by means of computational fluid dynamics. *Comput Chem Eng*. 1996;20:1467–1475.
11. Ghaniyari-Benis S, Hedayat N, Ziyari A, Kazemzadeh M, Shafiee M. Three-dimensional simulation of hydrodynamics in a rotating disc contactor using computational fluid dynamics. *Chem Eng Technol*. 2009;32:93–102.
12. Drumm C, Bart H-J. Hydrodynamics in a RDC extractor: single and two-phase PIV measurements and CFD simulations. *Chem Eng Technol*. 2006;29:1297–1302.
13. Weiss C, Bart H-J. Calculation of flow patterns in an RDC based on computational fluid-dynamic methods. In: Logsdail DH, Slater MJ, editors. *Solvent Extraction in the Process Industry*, Vol. 2. London: Elsevier Applied Science, 2003:1191–1197.
14. Bujalski JM, Yang W, Nikolov J, Solnordal CB, Schwarz MP. Measurement and CFD simulation of single-phase flow in solvent extraction pulsed column. *Chem Eng Sci*. 2006;61:2930–2938.
15. Retieb S, Guiraud P, Angelov G, Gourdon C. Hold-up within two-phase countercurrent pulsed columns via Eulerian simulations. *Chem Eng Sci*. 2006;62:4558–4572.
16. You X, Xiao X. Simulation of the three-dimensional two-phase flow in stirred extraction columns by Lagrangian–Eulerian method. *Chem Biochem Eng Q*. 2005;19:1–11.
17. Vikhansky A, Kraft M. Modeling of a RDC using a combined CFD-population balance approach. *Chem Eng Sci*. 2004;59:2597–2606.
18. Wang F, Mao Z-S. Numerical and experimental investigation of liquid–liquid two-phase flow in stirred tanks. *Ind Eng Chem Res*. 2005;44:5776–5787.
19. Drumm C, Attarakih MM, Bart H-J. Coupling of CFD with DPBM for a RDC extractor. *Chem Eng Sci*. 2009;64:721–732.
20. Drumm C, Tiwari S, Kuhnert J, Bart H-J. Finite pointset method for simulation of the liquid–liquid flow field in an extractor. *Comput Chem Eng*. 2008;32:2946–2957.
21. Kosters WCG. *Rotating disc contactor*. In: Lo TC, Baird MHI, Hanson C, editors. *Handbook of Solvent Extraction*. NewYork: Wiley, 1983.
22. Kompenhans J, Raffel M, Willert CE. *Particle Image Velocimetry—A Practical Guide*. Berlin: Springer, 1998.
23. Saarenrinne P, Piirto M. Turbulent kinetic energy dissipation rate estimation from PIV velocity vector fields. *Exp Fluids*. 2000;29: 300–307.
24. Baldi S, Ducci A, Yianneskis M. Determination of dissipation rate in stirred vessels through direct measurement of fluctuating velocity gradients. *Chem Eng Technol*. 2004;27:275–281.
25. Baldi S, Yianneskis M. On the quantification of energy dissipation in the impeller stream of a stirred vessel from fluctuating velocity gradient measurements. *Chem Eng Sci*. 2004;59:2659–2671.
26. Alekseenko SV, Bilsky AV, Dulin VM, Markovich DM. Experimental study of an impinging jet with different swirl rates. *Int J Heat Fluid Flow*. 2007;28:1340–1359.
27. Saarenrinne P, Piirto M, Eloranta H. Experiences of turbulence measurement with PIV. *Meas Sci Technol*. 2001;12:1904–1910.
28. Fluent Inc. *Fluent 6.3 User's Guide*. Lebanon: Fluent Inc, 2005.
29. Bahmanyar H, Slater MJ. Studies of drop break-up in liquid–liquid systems in a rotating disc contactor. Part I. Condition of no mass transfer. *Chem Eng Technol*. 1991;14:79–89.

Manuscript received Aug. 27, 2009, and revision received Feb. 6, 2010.